International Journal of Greenhouse Gas Control 114 (2022) 103607

Contents lists available at ScienceDirect

International Journal of Greenhouse Gas Control

journal homepage: www.elsevier.com/locate/ijggc

# Pore-scale bubble population dynamics of $CO_2$-foam at reservoir pressure

Benyamine Benali [a,*], Tore L. Føyen [a,b], Zachary Paul Alcorn [a], Malin Haugen [a], Jarand Gauteplass [a], Anthony R. Kovscek [c], Martin A. Fernø [a]

[a] Department of Physics and Technology, University of Bergen, Norway
[b] SINTEF Industry, Norway
[c] Department of Energy Resources Engineering, Stanford University, USA

ARTICLE INFO

*Keywords:*
$CO_2$ foam
Micromodels
Foam texture
CCUS
Quantitative pore-level analysis

ABSTRACT

The flow of $CO_2$ foam for mobility control in porous media is dictated by the foam texture, or bubble density, which is commonly expressed as the number of bubbles per unit of flowing gas. In most high-pressure laboratory studies of foam in porous media, the local foam texture cannot be determined due to opaque flow systems. Here, we unlock real-time foam texture dynamics at high pressure (100 bar) by utilizing a realistic pore network with an extended field of view. We identified snap-off as the dominant foam generation mechanism, with additional fining of foam texture caused by backward foam propagation. Foam coalescence during continuous $CO_2$ injection resulted in large gas channels parallel to the general flow direction that reduced the overall foam apparent viscosity. A large fraction of the $CO_2$ foam remained trapped ($X_t > 0.97$) and stationary in pores to divert $CO_2$ flow and increase sweep efficiency. The gas mobility was calculated from the fraction of trapped bubbles at the pore-scale, and the apparent foam viscosity agreed with similar injection test performed at core-scale. Hence, improved understanding of $CO_2$ foam texture evolution ($n_f$) can strengthen the validation of numerical foam models for upscaling of flow phenomena, instrumental in the development of field scale implementation of $CO_2$ foam for in carbon utilization and storage applications.

## 1. Introduction

Foam is a promising method for reducing $CO_2$ mobility in enhanced oil recovery (EOR) and $CO_2$ storage processes. $CO_2$ foam for mobility control can improve reservoir sweep efficiency, mitigate gravity override, and reduce viscous fingering for increased oil recovery (Enick et al., 2012) and $CO_2$ storage potential (Føyen et al., 2020). Foam is a thermodynamically unstable two-phase system of dispersed gas bubbles separated by continuous aqueous films (lamellae), stabilized by a foaming agent such as surfactant and/or nanoparticles. The geometry of the foam bubbles are dictated by the porous media they are contained within. Lamellae span entire pores, orthogonally to the general flow direction, reducing the mobility of gaseous phase. The aqueous phase remains continuous and is therefore unaffected by foam (Kovscek and Radke, 1994). Despite successful field-scale tests (Alcorn et al., 2019; Blaker et al., 1999; Chou et al., 1992), others have been unsuccessful (Stephenson et al., 1993) due injectivity issues and difficulty attributing additional displacement specifically to $CO_2$ foam, which is related to a limited understanding of foam generation, flow dynamics, and coalescence at reservoir conditions. Therefore, this study aims to unlock real-time foam dynamics at high pressure (100 bar) by utilizing a realistic pore network with an extended field of view.

Population balance foam models provide a mechanistic framework where the kinetics of foam generation and coalescence is mathematically expressed to track the number of foam bubbles (Kovscek et al., 1995). The number of bubbles in the system is used to calculate the mobility of the gas, however, the calculation is not straightforward. Crucial input in the calculation must be estimated, which is challenging in opaque cylindrical core plugs and sand packs. Such input includes quantifying the trapped gas fraction ($X_t$), which requires dual gas-phase tracer measurements (Tang and Kovscek, 2006). In addition, the texture of flowing foam bubbles ($n_f$), relies on measurements of produced foam which may not represent foam in porous media (Ettinger and Radke, 1992; Hou et al., 2013).

Foam is generated in porous media by three main mechanisms, including *Roof snap-off, lamella mobilization/division and lamella leave-behind* (Ransohoff and Radke, 1988; Rossen, 2003; Chen et al., 2005; Kovscek et al., 2007). The former two are considered prevailing mechanisms with lamellae orthogonal to flow direction and effective flow

* Corresponding author.
*E-mail address:* benyamine.benali@uib.no (B. Benali).

https://doi.org/10.1016/j.ijggc.2022.103607
Received 22 June 2021; Received in revised form 4 February 2022; Accepted 5 February 2022
Available online 12 February 2022

**Abbreviation and Nomenclature**

Carbon dioxide $CO_2$
field of view FoV
PV Pore volume
foam representative elementary volume foam-REV
Permeability $k$
Effective gas-foam relative permeability $k_{rg}^f$
Gas viscosity $\mu_g$
Effective viscosity of flowing foam $\mu_g^f$
Superficial gas flow velocity $u_g$
Foam apparent viscosity $\mu_{app}$
Gas pressure gradient $\nabla p_g$
Gas saturation $S_g$
Flowing gas saturation $S_{fg}$
Trapped gas saturation $S_{tg}$
Flowing bubble density $n_f$
Trapped bubble density $n_t$
Total number of bubbles $N_{bubble}$
Baseline number of bubbles $N_{baseline}$
Initial number of bubbles before foam coalescence $N_o$
mean bubble area A
trapped gas fraction $X_t$
System dependent scaling constant $\alpha$

impediment (Kam and Rossen, 2003). The third mechanism results in lamellae oriented parallel to flow direction, and an ineffective continuous gas foam (Friedmann et al., 1991; Kovscek and Radke, 1994). Several studies have suggested that a minimum threshold pressure gradients (or minimum flow velocities) need to be exceeded for foam generation to be initiated (Ransohoff and Radke, 1988; Rossen and Gauglitz, 1990; Rossen et al., 1994; Gauglitz et al., 2002). The existence of minimum threshold pressure gradients can have unfavorable consequences for foam generation and propagation far from injection wells, where the pressure gradients are low. However, foam can be generated by *Roof snap off* independent of pressure gradients at sharp increases in permeability (Rossen, 1999; Shah et al., 2019). During foam flow the pressure gradients can vary and fluctuate in space and time, resulting in local pressure gradients for the creation of lamellae (Kam and Rossen, 2003). Positive feedback processes can also occur during foam generation because foam increases the pressure gradients and subsequently causes the generation of more foam (Føyen et al., 2020).

Foam coalescence reduces the number of bubbles in porous media by three mechanisms: coarsening by diffusion (Ostwald ripening), capillary suction drainage (Kovscek and Radke, 1994) and gravitational liquid drainage. Coarsening by diffusion occurs due to the transport of gas from smaller bubbles (small radius, high curvature), with a higher internal pressure, to larger bubbles with lower internal pressure, causing the smaller bubbles disappear (Saint-Jalmes, 2006; Marchalot et al., 2008). Capillary suction drainage occurs when the water saturation approaches a saturation value where the lamellae are no longer stable, because the capillary pressure exceeds the maximum disjoining pressure of the foam film and drains the lamellae (Jiménez and Radke, 1989; Falls et al., 1989; Farajzadeh et al., 2015).

Gas mobility reduction by foam is caused by increased effective gas viscosity ($\mu_g^f$) and decreased effective gas relative permeability ($k_{rg}^f$). The combined effect can be assessed by adapting Darcy's law for foam flow (Kovscek and Radke, 1994).

$$u_g = \frac{k k_{rg}^f \nabla \mathrm{p_g}}{\mu_g^f} \tag{1}$$

where $u_g$ is the superficial gas flow velocity, $k$ is the absolute permeability, $k_{rg}^f$ is the effective gas-foam relative permeability, $\mu_g^f$ is the effective viscosity of flowing foam and $\nabla p_g$ is the gas pressure gradient.

Most quantification of foam strength relies on the measured pressure gradient. However, the pressure gradient depends on flow velocity ($u$) and absolute permeability ($k$), which lack generality, often making it unsuitable for comparison purposes. Foam apparent viscosity ($\mu_{app}$) accounts for differences in absolute permeability and flow velocity and is commonly reported:

$$\mu_{app} = \frac{k}{u} * \nabla \mathrm{p_g} \tag{2}$$

For foam flowing through the same pores where individual bubbles are constantly coalesced and regenerated (Ettinger and Radke, 1992), the effective gas viscosity increases. The increased effective gas viscosity is caused by the viscous shear when lamellae move along pore walls (Hirasaki and Lawson, 1985) and through pore throats (Falls et al., 1989). The effective viscosity of flowing foam ($\mu_g^f$) is proportional to the bubble density ($n_f$) (Kovscek and Radke, 1994; Fried, 1961), and is typically shear-thinning with respect to interstitial velocity ($v_f$), and can be described by (Kovscek et al., 1995):

$$\mu_g^f = \mu_g + \alpha * \frac{n_f}{v_f^c} \tag{3}$$

where $\mu_g$ is the gas viscosity, $\alpha$ is a system dependent scaling constant and $c$ has been estimated to be approximately 1/3 (Hirasaki and Lawson, 1985).

In addition to increasing the effective gas viscosity, trapped foam reduces the gas-foam relative permeability ($k_{rg}^f$). The flowing bubble trains will occupy the largest pores (Radke and Gillis, 1990) and a (Stone, 1970) model for three-phase relative permeability is applicable to estimate the effective gas-foam relative permeability. By considering the flowing ($S_{fg}$) and trapped ($S_{tg}$) gas as two pseudo saturations, we have a three-phase system, with water as the third phase which is most wetting and the flowing gas-foam is the least wetting phase. The relative permeability of the least (and most) wetting phase depends only on its own saturation and is the same as its two-phase relative permeability. Therefore, the effective gas-foam relative permeability ($k_{rg}^f$) equals the no-foam gas relative permeability at the flowing gas saturation $S_{fg}$ (Kovscek and Radke 1994).

The trapped gas fraction, $X_t$, is commonly used to compute the trapped gas saturation ($S_{tg}$) from gas saturation ($S_g$):

$$X_t = \frac{S_{tg}}{S_g} \tag{4}$$

Continuous-gas foam occurs when lamella generation becomes insufficient to maintain bubble densities, resulting in gas flow mainly through one or several interconnected channels not impeded by lamellae (Falls et al., 1989). The mobility reduction will be less compared to discontinuous foam because $n_f = 0$. However, the trapped bubbles will still reduce the mobility of the moving gas, as the gas-foam relative permeability ($k_{rg}^f$) is reduced.

Direct visual observation using microscopy during flow of fluids through porous media can be obtained using two-dimensional flow cells termed micromodels. Micromodels allow observation and characterization of individual fluid bubbles or ganglion and are particularly useful for foam studies for a range of important foam phenomena including generation (Géraud et al., 2017; Kovscek et al., 2007), coarsening (Jones et al., 2018a; Marchalot et al., 2008), texture (Rognmo et al., 2019; Rangel-German and Kovscek, 2006), gas trapping (Lv et al., 2018; Jones et al., 2018b), flow (Géraud et al., 2016) and flow diversion

(Khoshkalam et al., 2019; Gauteplass et al., 2015). Most microfluidic studies investigated decoupled foam phenomena in a limited field of view (FoV), whereas a complete assessment of foam in porous media requires combined observations of foam generation, coarsening, and texture.

This work presents a comprehensive laboratory investigation of essential foam features and phenomena during dynamic flow at reservoir conditions over a representative area, supported by the framework developed for population balance foam models. In addition, we investigate the foam generation and stabilization when adding nanoparticles at two different concentrations (150 and 1500 ppm) to the foaming solution.

## 2. Materials and methods

### 2.1. Fluid preparation

Brine (3.5 wt.% NaCl) was used for all aqueous phases (Table 1) and was filtered through a 0.45 μm cellulose acetate filter to remove particles before mixing with other components or injected it through the micromodel. Two foaming agents were used: Surfonic L24-22A (a non-ionic surfactant with linear ethoxylated alcohol, Huntsman), and Levasil CC301 (a surface-modified spherical silica nanoparticle, Nouryon). Three foaming solutions were prepared by mixing brine with surfactant, nanoparticle or a hybrid combination of both (Table 1). $CO_2$ of 99.999% purity was used during the micromodel foam injections. The pore space was cleaned between each injection cycle using 2-propanol-water azeotrope (IPA).

### 2.2. Micromodel and holder

The micromodel consists of an etched silicon wafer with a realistic porous structure bonded to an optically transparent borosilicate glass. The chemical characteristics of crystalline silicon (silicon wafer) and borosilicate glass are similar to sandstone (mainly quartz), which are chemically inert to injected fluids. Deep reactive ion etching resulted in vertical pore walls and sharp edges, resembling grain shapes found in real reservoir rocks generated from Berea sandstone thin sections. However, when 3D porous media in a real reservoir rock is simplified to 2D, some modifications were made to the pattern to connect pores which were isolated, resulting in higher permeability and porosity relative to Berea sandstone. Complete production procedures can be found in (Buchgraber et al., 2012). The rectangular porous pattern (27 mm X 21.40 mm) was equipped with flow ports in each corner, with inlet and outlet fluid distribution channels (200 $\mu m$ width) that connected ports 1 and 2, and ports 3 and 4 (Fig. 1). The porous pattern (27,000 grains) constitutes 36 (4 × 9) repetitions of pore network with 749 unique grains with shapes from a thin-section image of natural sandstone; a rock type extensively used in laboratory studies of oil production, foam and $CO_2$ storage. The porous pattern can be considered as a simplified two-dimensional projection of real pore structures, with connected pores that allow flow and discontinuous, irregularly shaped grains that provide flow tortuosity.

Micromodel properties are listed in Table 2. The porosity was quantified as the ratio of areal pore space to the total area (grains + pore space) and was calculated to be 0.61 from a stitched, high-resolution images of the whole porous pattern. The pore volume (PV) with constant etching depth of 30 $\mu m$ was 11.1 $\mu L$ . The grain size distribution of the unique pattern with 749 grains ranged between 100 to 79 000 $\mu m^2$ and the pore throat (defined as the shortest pore space distance between two adjacent grains) distribution ranged between 10 to 300 $\mu m$ (Fig. 1). The constant etching depth resulted in square- or rectangular-shaped pore throat cross-sections. The absolute permeability of the micromodel was 2.97 D.

The micromodel was positioned in a depression in the bottom part of the two-part aluminum micromodel holder with flow ports aligned with threaded connections sealed with O-rings. The top part, with an open window for direct observation, was attached to the bottom with eight screws using 0.20 Nm force. The system can be pressurized to 150 bar without external confinement pressure.

**Table 1**
Composition of aqueous solutions.

| Aqueous Solution | Concentration, *Component* |
|---|---|
| Brine | **35,000 ppm,** *NaCl in distilled water* |
| SF5000 | **5000 ppm,** *Surfonic L24–22* |
| SF5000 + NP1500 | **5000 ppm,** *Surfonic L24–22,* + **1500 ppm,** *Levasil CC301* |
| SF5000 + NP150 | **5000 ppm,** *Surfonic L24–22,* + **150 ppm,** *Levasil CC301* |
| IPA | **877,000 ppm,** *2-propanol in distilled water* |

### 2.3. Experimental setup and procedure

The micromodel holder was positioned on a motorized scanning stage below the microscope (Axio Zoom. V16, Zeiss) equipped with a diffuse ring-illuminator. The microscopic zoom, focus, illuminator intensity, imaging, and the motorized stage was controlled with the Zeiss proprietary software. Microscope settings (light intensity, aperture and shutter time) were optimized for image processing and kept constant for all experiments. The software performed shading corrections and focus adjustments for any misalignments. Fluid injection and production utilized a series of valves and pumps (Fig. 2) and the pore pressure was kept at a minimum of 100 bar using a backpressure system. The injected and produced fluids were considered incompressible at the system temperature (ambient), and pressure gradients during flow (tens of millibars) were not expected to change fluid properties and flow rates. Four unsteady state $CO_2$ injections were performed (three with foaming solutions listed in Table 1, and one using brine for baseline) using the following procedure:

i Pre-saturate the micromodel with foaming solution
ii Inject dense phase $CO_2$ at a constant volumetric flow rate (4 $\mu L/min$) into port1 with port 2 closed and ports 3 and 4 open and kept at 100 bars using the backpressure system.

### 2.4. Image processing and analysis

The motorized scanning stage and software enabled imaging of the entire porous pattern (27 mm X 21.40 mm) with high spatial resolution (4.38 μm/pixel) by stitching multiple overlapping images (Fig. 1). Image acquisition time of the porous pattern (121 separate images) was 1 min 13 s and time-lapsed series captured the position of each individual foam bubble every 1 min 15 s. The following three-step image segmentation process was performed:

Thresholding the images using a low (dark) threshold value by utilizing the significantly darker colored grain structure compared to the pore space. The grains were then drawn black on a white empty image.
Thresholding the images using a high (bright) threshold value by utilizing the white colored (due to the diffuse ring-illuminator) gaseous-aqueous interfaces and grain walls. The bright areas were then painted black on the white empty image.

The rest of the white empty image is the discrete bubbles. This resulted in a binary image with grains, grain walls and gaseous-aqueous interfaces as black, and discrete bubbles as white.

The final segmented image (Fig. 3) shows the discrete bubbles colored red and grains colored blue for illustrative purposes. The bubbles were further described using functions available in the Python library OpenCV (Bradski 2000) as continuous contours with the following features: center of mass (coordinates), area, perimeter length,

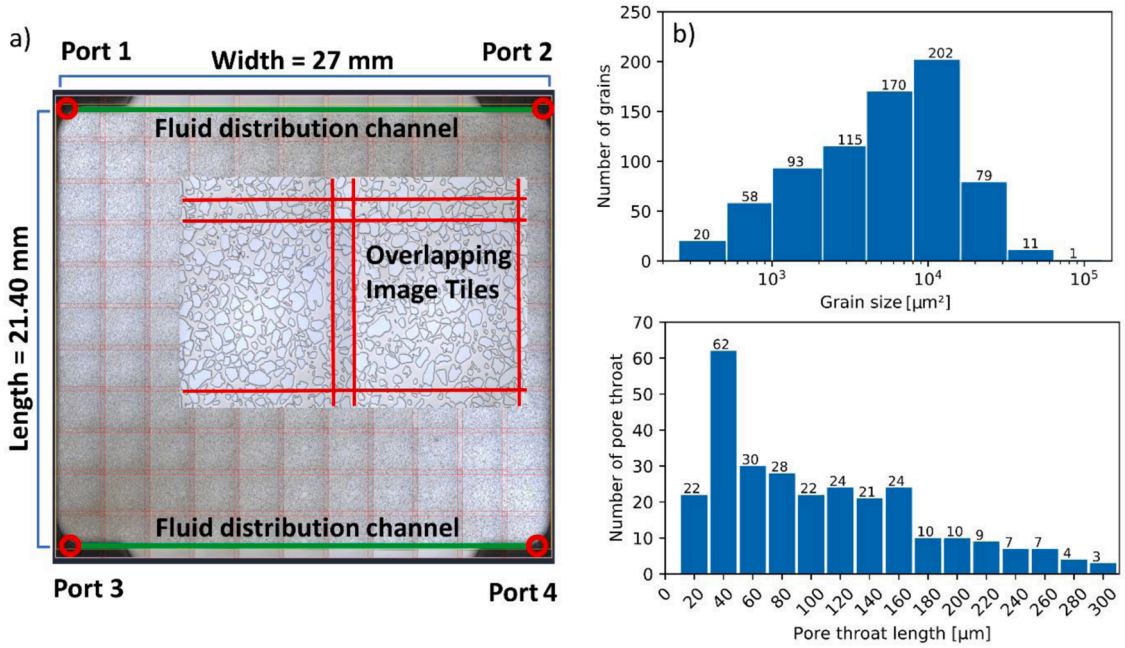


**Fig. 1.** Right: Dimensions of porous pattern in micromodel, location of flow ports and fluid distribution channels. The overlapping image acquisition titles (121 in total) are shown using red lines above the porous pattern (exaggerated for illustration purposes). Left: Characteristic features of the micromodel from one of the 36 repetitions of the pattern, grain size distribution (top) and pore throat length distribution (bottom). Average pore throat length was 89 μm.

**Table 2**
Micromodel properties.

| Parameter | Value |
|---|---|
| Width | 27 *mm* |
| Length | 21.40 *mm* |
| Depth | 30 *μm* |
| Porosity | 0.61 |
| Permeability | 2.97 D |
| Pattern repetition | 36 |
| Unique grains | 749 |
| Total grains | 27,000 |
| Grain size | 100–79,000 $\mu m^2$ |
| Pore throat length | 10–300 *μm* |

orientation, bounding boxes, and minimum enclosing ellipse with minor and major axis. These characteristics were used in the analysis of foam flow and bubble generation/coalescence.

## 3. Results and discussion

Pore-scale foam flow phenomena were studied using temporal bubble density mapping, bubble number ($N_i$) and bubble size during foam generation and coalescence. Temporal bubble numbers during foam generation and coalescence ($N_{bubble}$) were normalized to the baseline ($N_{baseline}$) for three foaming solutions (Fig. 4). $N_{baseline}$ increased linearly from 1000 to 1850 in the first 10 PVs then kept increasing linearly at lower rate to 3000 bubbles at PV 60. Foam generation increased N to approximately 40 to 50 times of the baseline, reaching peak values after approximately 5 PV of $CO_2$ injected. When increasing the nanoparticles

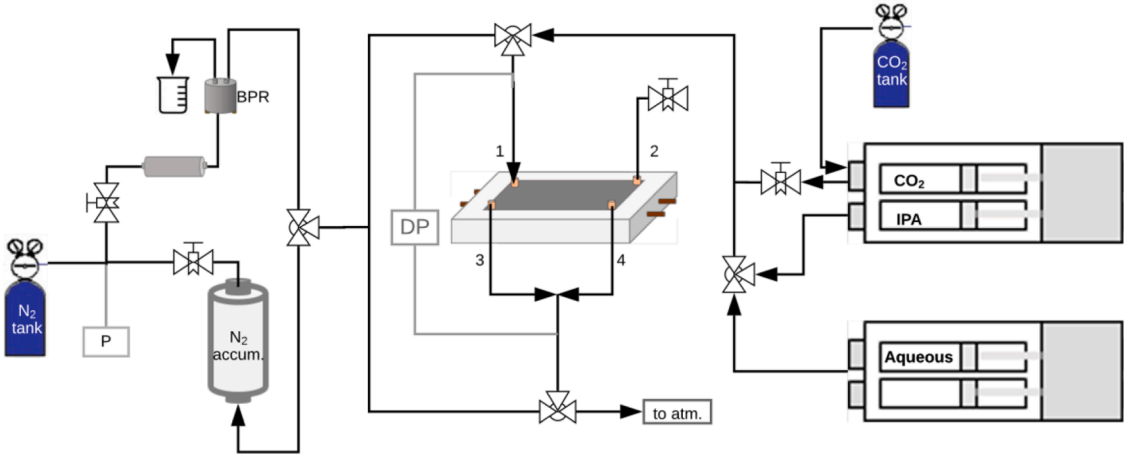


**Fig. 2.** Experimental setup used for the pore-scale foam studies using etched-silicon wafer micromodels. The micromodel holder was positioned underneath the microscope (not shown). Two high precision plunger pumps (Quizix Q5000-2.5 K and Quizix Q5000-10 K) were used for fluid injection. The Q5000-2.5 K pump was used in single cylinder injection mode, with $CO_2$ and cleaning solvents (IPA) in each of the two cylinders, whereas the Q5000-10 K was solely used for injection of surfactant. The $N_2$ accumulator tank was used to regulate the backpressure: a 1 L pressure vessel was filled with $N_2$ and received the produced fluids (water and dense liquid $CO_2$) during injections. The produced fluids were vented from the pressure vessel during the preparation between the micromodel foam experiments.

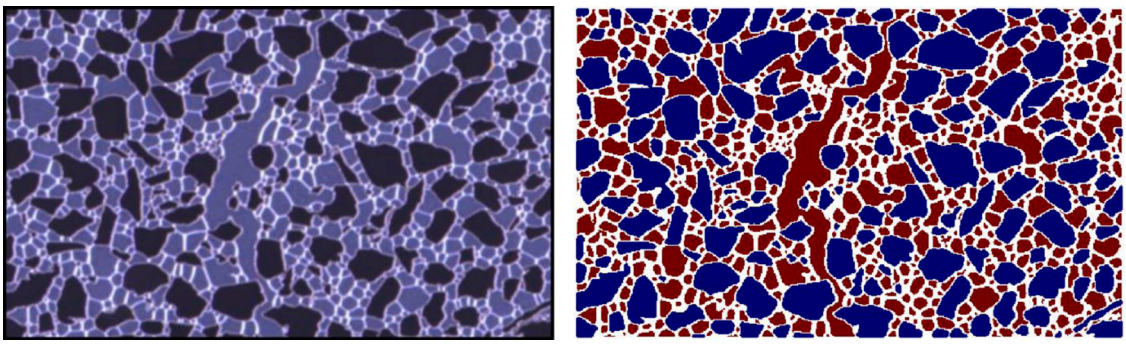

**Fig. 3.** Illustration of the segmentation process. Left: Raw image (2.2 mm x 1.3 mm) of the micromodel with foam occupying the porous pattern. Right: Segmented image, blue areas are the grain structure, red areas are discrete foam bubbles.

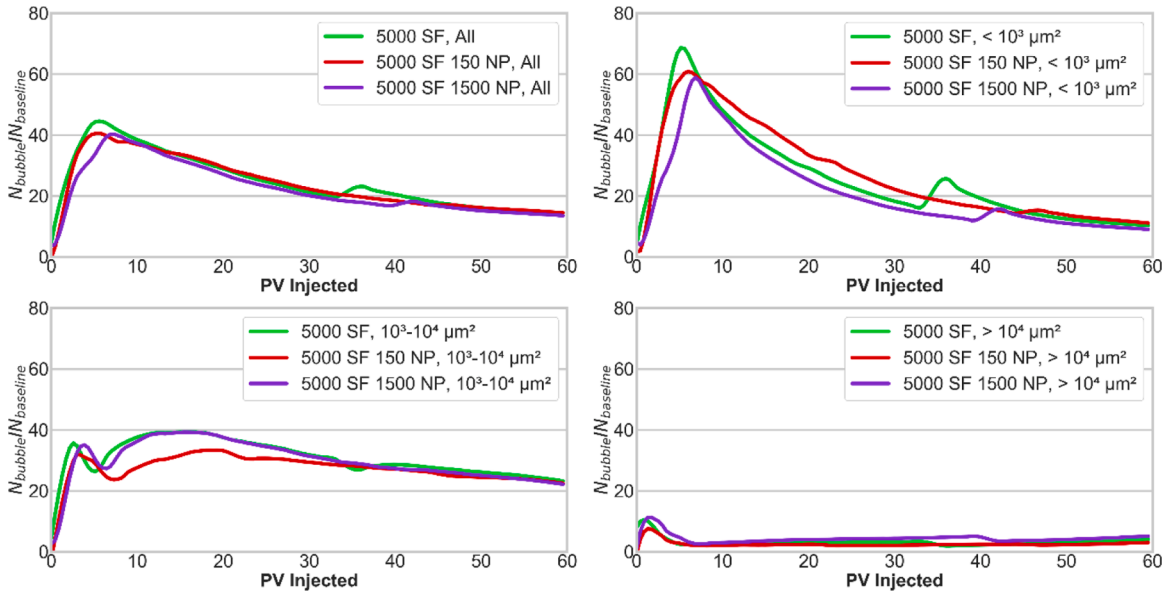


**Fig. 4.** Development in normalized bubble number (with respected to the baseline). The bubbles are sorted into logarithmical bubble size groups: a) all bubbles; b) small bubbles with area $< 10^3 \mu m^2$; c) intermediate bubbles with area between $10^3$to $10^4 \mu m^2$; d) large bubbles with area $> 10^4 \mu m^2$. Sorting the number of bubbles based on size shows that the number of intermediate size bubbles are increasing at the expense of small bubbles after 5 PV of $CO_2$ injection. The baseline and the foam injections are smoothed with a running average of 51 and 11, respectively.

concentration, we observe that N peak for small bubbles was delayed and lower compared to the other foaming solution (Fig. 4 top right). Bubble coarsening (decreased N) was the dominating coalescence mechanism. The foam generation and stabilization overall were not affected by adding nanoparticles to the foaming solution as the temporal bubble numbers for the three injections had same trend. Detailed discussion of results from foam generation (3.1), foam flow (3.2), and foam decay (3.3) is below.

### 3.1. Foam generation

Foam generation occurred primarily by snap-off in regions with sufficient liquid saturation and sharp constrictions between pore throats and bodies. Subsequent flow diversion increased $CO_2$ flow velocity locally, resulting in additional foam generation. Bubble density maps initially show low foam generation with a rapid increase when the injected $CO_2$ reached the outlet flow channel between 0.4 and 1.3 PV $CO_2$ injected (**Fig. 5**). This resulted in backward (from outlet to inlet) foam propagation previously reported and attributed to foam becoming stronger (Simjoo and Zitha, 2020; Almajid et al., 2019; Apaydin and Kovscek, 2001). As mentioned in the previous section, we observe also in bubble density maps that foam generation was delayed when increasing the nanoparticles concentration, the reason for this phenomenon may be related to the aggregation of NP. The determining mechanisms for foam strengthening are not clear, and it has hypothesized to occur by foam transitioning from weak to strong state, or by favorable conditions for snap-off due to the end effect in the permeability transition zone. Backward propagation of the foam front does, however, indicate that snap-off was the prevailing generation mechanism during the initial period because lamella mobilization and division is a secondary generation mechanism that requires the presence of foam and can only result in forward-propagation. The secondary generation mechanism may have contributed to refinement of the foam texture and regeneration to increase bubble densities after the initial period. The observed foam behavior is likely important for long-distance foam generation where pressure gradients are likely to be small (Hirasaki et al., 1997; Szafranski et al., 1998). Foam generation at sharp permeability contrasts can also occur some distance from the injection well at lower pressure gradients if sufficient foaming solutions are available. Additionally, super-linear increases in apparent viscosity during core scale unsteady state experiments, indicate that positive feedback behavior (Føyen et al., 2020) is likely related to the backward propagation mechanism observed at the pore-level.

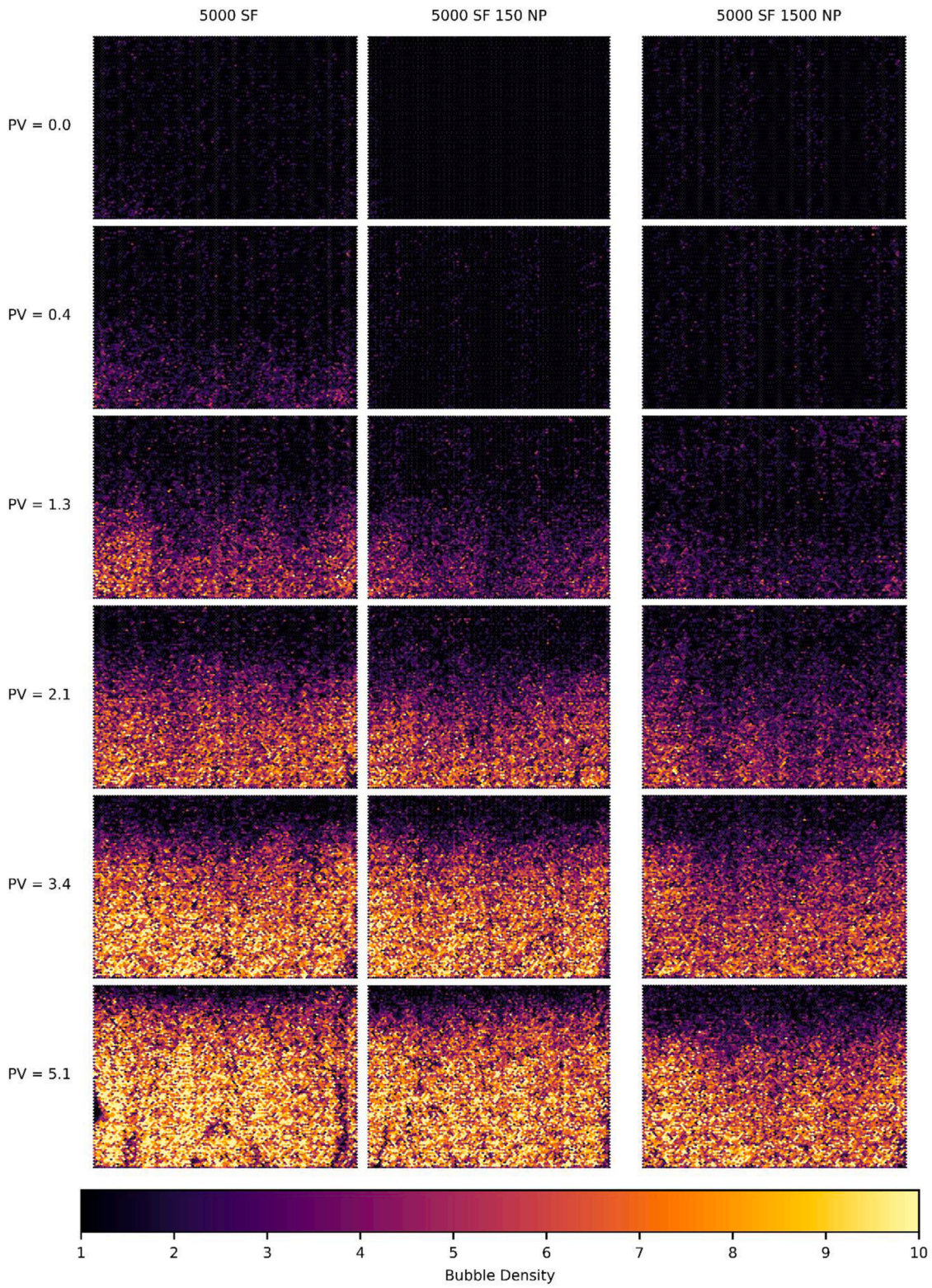


**Fig. 5.** Bubble density mapping during foam generation (up to 5 PV of $CO_2$ injection) for three foam solutions listed in Table 1. Foam generation initiated between 0.4 and 1.3 PV of $CO_2$ injected at the sharp permeability contrast (outlet flow channel, bottom side of density maps), resulting in higher foam density (brighter color) in the outlet regions of porous pattern. Foam propagated backwards (outlet to inlet) resulting in higher foam density through the micromodel. The resolution of the spatially resolved hexagonal binning plot is 150 × 90.

### *3.2. Flowing and trapped foam*

Flowing regions were characterized by moving bubble trains and continuous gas channels. Movement of bubble trains occurred with temporary flow suspension, restart and randomly relocated (Fig. 6). Open gas channels extended several pore lengths and emerged from inadequate upstream bubble regeneration to replace displaced bubbles downstream. Open channels were irregularly filled with bubbles and

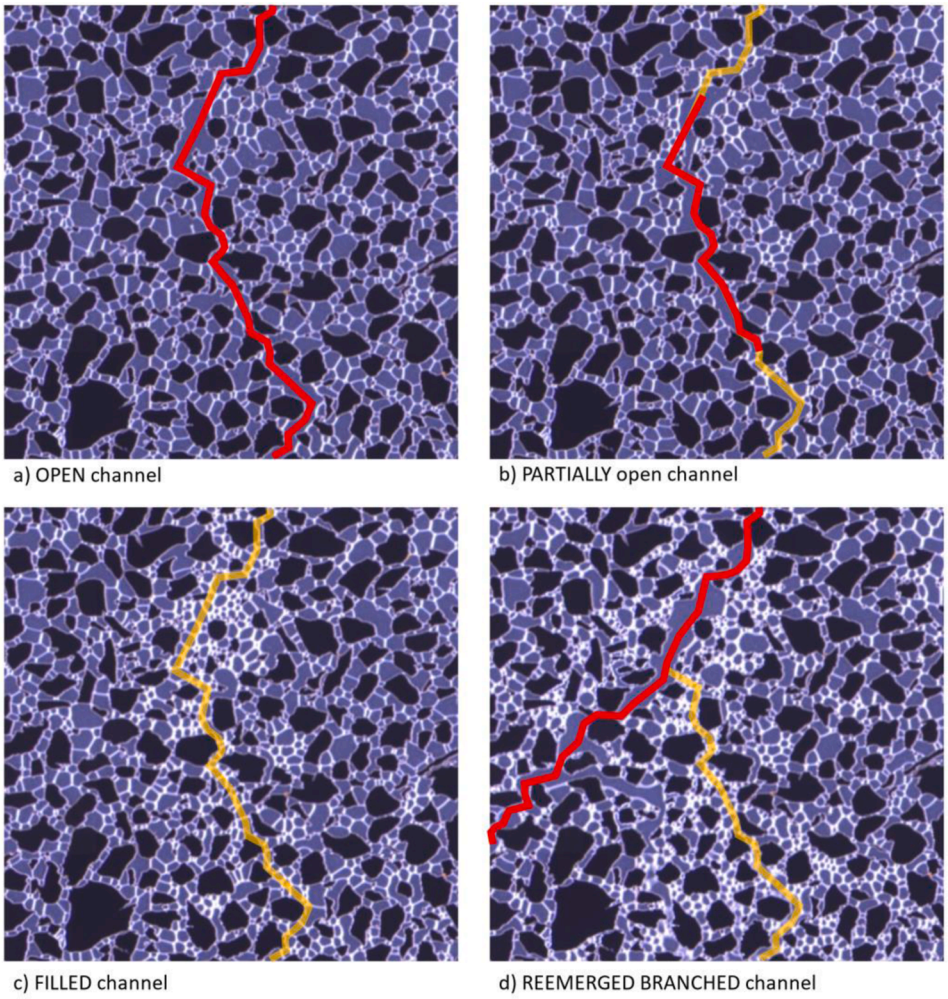


**Fig. 6.** Dynamics of open gas channels during bubble generation: red indicates path of an open channel (without bubbles) and orange indicates where the open channel fills with bubbles. Sequential images show: a) path of an open channel ($t = 33.8$ PV); b) channel becomes partially open ($t = 34.2$ PV); c) channel becomes filled with bubbles ($t = 34.7$ PV); d) a new path emerges that branches from the original path, now partially filled with bubbles ($t = 35.1$ PV). The images are from the SF5000 injection at the same field of view (2.2 mm x 2.2 mm).

reemerged in the same or new pathways. Trapped bubbles adjacent to open or partially filled channels changed from low energy configuration (no curvature, image a) to texture with less capillary resistance (with curvature, images c and f). The observation of large regions of trapped bubbles support that lamellae moving to a minimum energy configuration (at rest) will have a greater capillary resistance to remobilization (Jones et al., 2018a; Hou et al., 2013). Hence, the lamella in stationary regions will not move when exposed to the same pressure gradient as the lamella in the flowing region.

The density of the flowing bubbles ($n_f$) is used to calculate the effective gas viscosity in population balance foam models and is commonly assumed to be equal to the density of trapped bubbles ($n_t$) (Kovscek and Radke, 1994). With a limited field of view (2 mm x 2 mm, Fig. 6), assessment of local $n_f$ becomes ambiguous:

i In open channels (images a and d), the $CO_2$ flow is not impeded by bubbles and $n_f = 0$, *i.e.* $n_f < n_t$.
ii In filled channels (image c, $n_f$ is higher than $n_t$ in surrounding region, *i.e.* $n_f > n_t$.
iii Partially filled channels (image b), $n_f$ is the mean value of the filled and the open part of the channel, and depends on the relative size between the two parts and the bubble density.

Hence, a foam representative elementary volume (foam-REV) must be defined that provides a $n_f$ representative for the whole system (Hill, 1963). Dynamics of bubble density, gas channels, flowing bubbles and trapped bubbles were therefore mapped in the entire pore space using hexagonal binning plot (Fig. 7). Open gas channels were defined as large bubbles exceeding a size of 25% of micromodel length. Flowing bubbles were identified by temporal changes in bubble position and size, individually determined for all bubbles: bubble position changed if the relocation exceeded 20% of its minor axis (defined by an enclosing eclipse) between time-lapse images, and bubble size changed if its area increased/decreased more than 20%. Temporal changes in bubble position and size and the position of open gas channels were based on observations between 5 image frames, corresponding to 1.7 PV $CO_2$ injected. Trapped bubbles (without change in position and size) were found by combining the bubble density and flowing bubble maps: *trapped = density / (flow +1)*. It is not known if the size of the whole porous pattern (27 mm x 21.40 mm) is sufficient to define foam-REV. Still, we observed that the length of the open channels remained constant for extended periods (Fig. 8). Therefore, when the relationship between flowing and stationary regions is constant, we can estimate a mean representative flowing bubble density.

The gas mobility in the presence of foam can be found with knowledge of trapped bubbles (reduced gas relative permeability) and moving bubble trains (increased effective gas viscosity). The latter can be ignored when open gas channels spanned the porous pattern Eq. (3) ($n_f = 0$) $\rightarrow \mu_g^f = \mu_g = 0.081\ cP$). Hence, gas mobility can be determined directly from the fraction of trapped gas ($X_t$), that is estimated from the open gas channel area (Fig. 8) or flowing region area (Fig. 7). Note that the flowing regions were determined over 1.7 PV and the fraction of trapped bubbles is underestimated due to the irregular relocation of bubble trains and continuous gas channels (Fig. 7). The gas mobility can

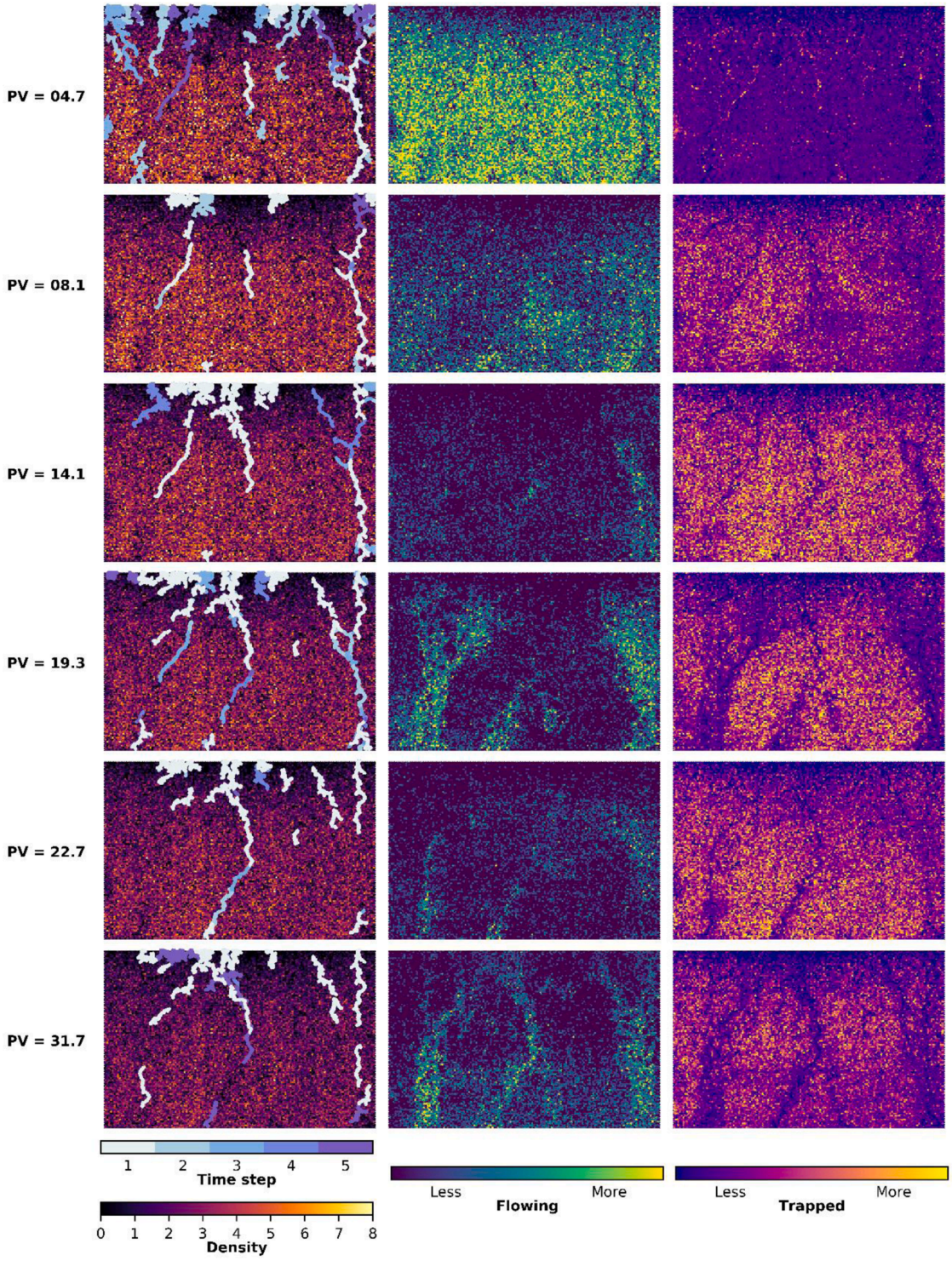


**Fig. 7.** Pore-scale foam dynamics with spatial bubble density, open gas channels, flowing bubbles and trapped bubbles using hexagonal binning plots (150 × 90) Left column: bubble density (number of bubbles in each hexagon) with mapped open gas channels (lines). Center column: flowing bubbles. Right column: Trapped bubbles. Location of open gas channels, flowing and trapped bubbles were calculated each 1.7 PV $CO_2$ injected. The micromodel was pre-saturated with the foaming solution (SF5000) prior to $CO_2$ injection (top to bottom).

be determined when most of the flow occurs in open gas channels because they can be used to estimate $X_t$ by subtracting the volume (area) constituting the open gas channels (Fig. 8): with open gas channels occupying between 0.75 to 1.75% of the pore space, $X_t$ ranged between 0.98 and 0.99 (assuming $S_g = 0.8$). As mentioned earlier, the effective gas-foam relative permeability equals the no-foam gas relative permeability at the flowing gas saturation, and by assuming a linear relationship between relative permeability and saturation, the gas-foam relative permeability ($k^f_{rg}$) can be calculated to range between 0.008 and 0.016. Foam apparent viscosity has been calculated using Eq. (1) and ((2) to range between 5.1 to 10.1 cP that corroborates core floods at similar conditions (Føyen et al., 2020).

The effective gas viscosity from bubble trains cannot be ignored when open gas channels do not span the porous pattern and must be

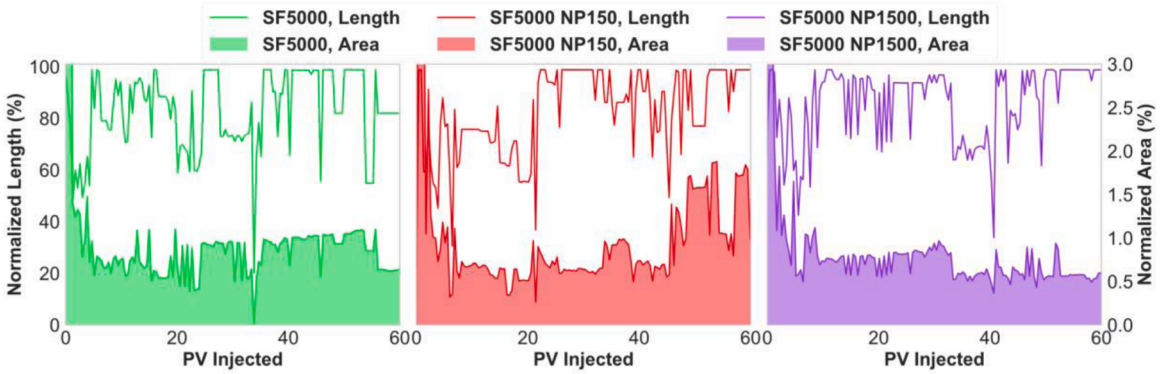


**Fig. 8.** Quantification of open gas channel length and area for three foaming solutions. The length is normalized between inlet (0%) and outlet (100%) using solid lines. Channel area (filled region) is normalized to pore space when the channel length exceeds 25%.

considered to assess the gas mobility reduction for such cases using Eq. (1). Direct quantification is not obtainable from the images because the parameter $\alpha$ that depends on the foaming system and germination sites (Pancharoen et al., 2012) cannot be estimated from the unsteady state injections reported here. However, adequate measured differential pressure can potentially be used to estimate $\alpha$, which is a parameter used in population balance modeling (Kovscek et al., 1995; Eide et al., 2020). Direct quantification of $\alpha$ by micromodel studies can, therefore, be valuable for foam agent screening, as it is less time consuming than core floods, and can be used as input for population balance modeling.

### 3.3. Foam decay

Foam coalescence became dominant at later times (after approximately 5 PV of $CO_2$ injected, Fig. 4) with overall decreasing bubble numbers. We rank coalescence mechanisms in our porous media from the three known bubble coalescence mechanisms: *i.* coarsening by diffusion (Ostwald ripening), *ii.* liquid film drainage by capillary or gravity forces, and *iii.* gravitational liquid drainage. From the observed flow pattern changes due to foam regeneration (discussed in detail below) we conclude that capillary liquid film drainage is not prevailing because it requires low liquid saturations not consistent with observations. Gravitational liquid drainage is considered negligible in the horizontally oriented system with 30 $\mu m$ etching depth. Therefore, we consider Ostwald ripening the prevailing coalescence mechanism, where intermediate-sized bubbles increased at the expense of smaller bubbles (Fig. 4). Smaller bubbles disappeared due to diffusive gas transport from bubbles with higher Laplace pressure (small bubble radii) to bubbles with lower Laplace pressure (high bubble radii). Fick's law determines diffusion rate, and it is expected that Ostwald ripening will depend on time. The development in bubble number and mean bubble area (A) agrees with Von Neumann's law (Saint-Jalmes, 2006; Marchalot et al., 2008) that describes coarsening in trapped two-dimensional foam (Fig. 9). The development in mean bubble area and the ratio $N_o/N(t)$ scales linearly with time (PV injected), where $N(t)$ is the number of bubbles at a time $t$ and $N_0$ is the initial number of bubbles before foam coalescence becomes dominant. $N_o$ is the greatest observed bubble number and marked the transition between when the rate of foam coalescence exceeded rate of foam generation. The transition can be recognized when $N_o/N(t) = 1$ (after approximately 5 PV $CO_2$ injected), and the relationship $N_o/N(t)$ increases as the foam texture becomes coarser. We focus our foam coarsening analysis between 5 and 30 PV injected as foam was regenerated between 35 and 45 PV injected, likely caused by mobilization of foaming solution from system dead ends.

In trapped, two-dimensional foams, coarsening is expected to stop when foam lamellae are located at the pore-throats with zero curvature, *i.e.* equal bubble pressures without pressure gradients to drive further diffusion and coarsening (Jones et al., 2018a). Hence, $A$ and $N_o/N(t)$ scale with time only during a limited initial coarsening period (Jones et al. (2018a) reported 1500 s), before the lamellae come to rest at the pore throats. The presence of large gas channels and slow foam regeneration sustained foam coarsening from approximately 5 PV $CO_2$ injected. The presence of large gas channels spanning several pores observed in our system (Fig. 9) were effectively large bubbles with lower pressure than surrounding bubbles that promoted sustained Ostwald ripening. The prolonged coarsening caused the mean bubble areas for the three injections to increase in an average sense as 44 $\mu m^2$ per PV injected over minimum 25 PV (4125 s). The rate of increase was 0.26 $\mu m^2 s^{-1}$, compared with 1.14 $\mu m^2 s^{-1}$ for two-dimensional trapped foam during a limited initial coarsening period (Jones et al., 2018a). The difference

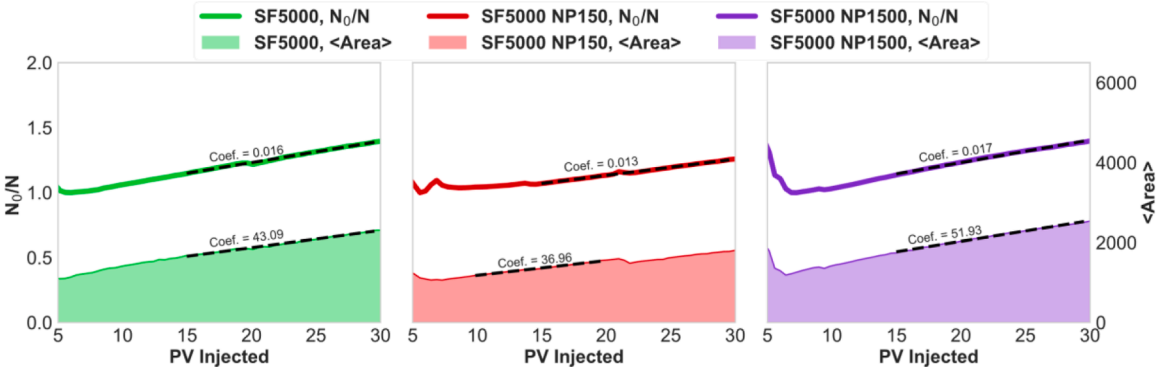


**Fig. 9.** Increasing $N_o/N(t)$ with decreasing number of bubbles (*left axis, solid line*) and increasing mean bubble area $\langle A \rangle$ (*right axis, filled area*) during foam coalescence by Ostwald ripening for three foaming solutions. Both the mean bubble area and the ratio $N_o/N(t)$ scaled linearly with time (PV injected) and agrees with Von Neumann's law for two-dimensional foams. The associated regression coefficient (slope) are included on top of the curves.

between stationary and flowing systems is expected as regeneration of foam does not occur in a stationary system. Additionally, different gases and pressures were used, and the solubility of the gaseous phase in aqueous phase influence diffusion and subsequent coarsening.

## 4. Conclusions

Bubble flow, texture and trapping dynamics for dense $CO_2$ foam were studied at high pressure at the pore scale using a realistic pore network. The aggregated effect of foam generation, coarsening, and texture was contextualized through the population balance model framework. Roof snap-off at sharp permeability contrasts was the dominant foam generation mechanism with additional refining of foam texture caused by backward foam propagation. Coarsening during continuous $CO_2$ injection occurred due to Ostwald ripening. Foam generation and stabilization were not affected by adding nanoparticles to the foaming solution. Flowing regions were characterized by moving bubble trains and open gas channels. Stationary regions with trapped foam had a greater capillary resistance than moving bubble trains. The gas mobility in the presence of open gas channels and trapped bubbles was estimated by quantifying the fraction of trapped bubbles, corresponding to an apparent foam viscosity between 5.1 to 10.1 cP. Assessment of foam texture ($n_f$ and $n_t$) needs to be performed over a significantly large area of the porous pattern to define a foam representative elementary volume.

## Data availability

The foam injection datasets, including segmented images, used during the current sturdy are available at https://doi.org/10.17632/5d37nbzf9s.1, an open-source online data repository hosted by Mendeley Data (Benali and Føyen, 2020). The raw foam injection micromodel images are available from the corresponding author on reasonable request.

## CRediT authorship contribution statement

**Benyamine Benali:** Conceptualization, Methodology, Software. **Tore L. Føyen:** Conceptualization, Methodology, Software. **Zachary Paul Alcorn:** Writing – review & editing, Supervision. **Malin Haugen:** Methodology. **Jarand Gauteplass:** Conceptualization, Writing – review & editing. **Anthony R. Kovscek:** Writing – review & editing. **Martin A. Fernø:** Conceptualization, Writing – review & editing, Supervision.

## Declaration of Competing Interest

The authors declare that they have no known competing financial interests or personal relationships that could have appeared to influence the work reported in this paper.

## Acknowledgement

The authors wish to acknowledge the Research Council of Norway for financial support (project no. 249742, 268216, 294886 and 301201) for funding of PhD candidate Benyamine Benali and Dr. Zachary Paul Alcorn, and support from Industry Partners Nouryon, Shell E&P, Total E&P, and Equinor

## References

Alcorn, Z.P., Fredriksen, S.B., Sharma, M., Rognmo, A.U., Føyen, T.L., Fernø, M.A., Graue, A, 2019. An integrated carbon-dioxide-foam enhanced-oil-recovery pilot program with combined carbon capture, utilization, and storage in an onshore texas heterogeneous carbonate field. SPE Reserv. Eval. Eng. 22 (04), 1449–1466. https://doi.org/10.2118/190204-pa.

Almajid, M.M., Nazari, N., Kovscek, A.R, 2019. Modeling steady-state foam flow: hysteresis and backward front movement. Energy Fuels. https://doi.org/10.1021/acs.energyfuels.9b01842.

Apaydin, O.G., Kovscek, A.R., 2001. Surfactant concentration and end effects on foam flow in porous media. Transp. Porous Media. https://doi.org/10.1023/A:1010740811277.

Benali, B., Føyen, T. Micromodel foam. In. Mendeley Data, (2020) </Dataset>.

Blaker, T., Celius, H.K., Lie, T., Martinsen, H.A., Rasmussen, L., Vassenden, .F., 1999. Foam for gas mobility control in the Snorre field: the FAWAG Project. In: Paper Presented at the SPE Annual Technical Conference and Exhibition. Houston, Texas. https://doi.org/10.2118/56478-MS.

Bradski, G., 2000. The opencv library. Dr Dobb's J. Softw. Tools 25 (5).

Buchgraber, M., Al-Dossary, M., Ross, C.M., Kovscek, A.R., 2012. Creation of a dual-porosity micromodel for pore-level visualization of multiphase flow. J. Pet. Sci. Eng. https://doi.org/10.1016/j.petrol.2012.03.012.

Chen, M., Yortsos, Y.C., Rossen, W.R., 2005. Insights on foam generation in porous media from pore-network studies. Colloids Surfaces A Physicochem Eng. Asp. https://doi.org/10.1016/j.colsurfa.2005.01.020.

Chou, S., Vasicek, S., Pisio, D., Jasek, D., Goodgame, J., 1992. CO2 foam field trial at North Ward-Estes. In: Paper Presented at the SPE Annual Technical Conference and Exhibition. Washington.

Eide, Ø., Fernø, M., Bryant, S., Kovscek, A., Gauteplass, J., 2020. Population-balance modeling of CO2 foam for CCUS using nanoparticles. J. Nat. Gas Sci. Eng. https://doi.org/10.1016/j.jngse.2020.103378.

Enick, R.M., Olsen, D.K., Ammer, J.R., Schuller, W., 2012. Mobility and conformance control for CO2 EOR via thickeners, foams, and gels–A literature review of 40 years of research and pilot tests. In: Paper Presented at the SPE Improved Oil Recovery Symposium, Tulsa. Oklahoma, USA.

Ettinger, R.A., Radke, C.J., 1992. Influence of Texture on steady foam flow in Berea sandstone. SPE Reserv. Eng. https://doi.org/10.2118/19688-PA.

Falls, A.H., Musters, J.J., Ratulowski, J., 1989. The apparent viscosity of foams in homogeneous bead packs. SPE Reserv. Eng. https://doi.org/10.2118/16048-PA.

Farajzadeh, R., Lotfollahi, M., Eftekhari, A.A., Rossen, W.R., Hirasaki, G.J.H., 2015. Effect of permeability on implicit-texture foam model parameters and the limiting capillary pressure. Energy Fuels. https://doi.org/10.1021/acs.energyfuels.5b00248.

Fried, A.N., 1961. Foam-Drive Process for Increasing the Recovery of Oil. In. University of North Texas Libraries, Washington D.C.

Friedmann, F., Chen, W.H., Gauglitz, P.A., 1991. Experimental and simulation study of high-temperature foam displacement in porous media. SPE Reserv. Eng. https://doi.org/10.2118/17357-PA.

Føyen, T., Brattekås, B., Fernø, M.A., Barrabino, A., Holt, T., 2020. Increased CO2 storage capacity using CO2-foam. Int. J. Greenh. Gas Control. https://doi.org/10.1016/j.ijggc.2020.103016.

Gauglitz, P.A., Friedmann, F., Kam, S.I., Rossen, W.R., 2002. Foam generation in homogeneous porous media. Chem. Eng. Sci. https://doi.org/10.1016/S0009-2509(02)00340-8.

Gauteplass, J., Chaudhary, K., Kovscek, A.R., Fernø, M.A., 2015. Pore-level foam generation and flow for mobility control in fractured systems. Colloids Surfaces A Physicochem. Eng. Asp. https://doi.org/10.1016/j.colsurfa.2014.12.043.

Géraud, B., Jones, S.A., Cantat, I., Dollet, B., Méheust, Y., 2016. The flow of a foam in a two-dimensional porous medium. Water Resour. Res. https://doi.org/10.1002/2015wr017936.

Géraud, B., Méheust, Y., Cantat, I., Dollet, B., 2017. Lamella division in a foam flowing through a two-dimensional porous medium: a model fragmentation process. Phys. Rev. Lett. https://doi.org/10.1103/PhysRevLett.118.098003.

Hill, R., 1963. Elastic properties of reinforced solids: some theoretical principles. J. Mech. Phys. Solids. https://doi.org/10.1016/0022-5096(63)90036-X.

Hirasaki, G.J., Lawson, J.B., 1985. Mechanisms of foam flow in porous media: apparent viscosity in smooth capillaries. Soc. Pet. Eng. J. https://doi.org/10.2118/12129-PA.

Hirasaki, G.J., Miller, C.A., Szafranski, R., Tanzil, D., Lawson, J.B., Meinardus, H., Jin, M., Londergan, J.T., Jackson, R.E., Pope, G.A., Wade, W.H., 1997. Field Demonstration of the Surfactant/Foam Process for Aquifer Remediation. In: Paper Presented at the SPE Annual Technical Conference and Exhibition, San Antonio, Texas.

Hou, J., Du, Q., Li, Z., Pan, G., Lu, X., Zhou, K., 2013. Experiments on foam texture under high pressure in porous media. Flow Meas. Instrum. https://doi.org/10.1016/j.flowmeasinst.2013.05.002.

Jiménez, A.I., Radke, C.J., 1989. Dynamic Stability of foam lamellae flowing through a periodically constricted pore. Oil-Field Chemistry, vol. 396. American Chemical Society, pp. 460–479. ACS Symposium Series, vol. 396.

Jones, S.A., Getrouw, N., Vincent-Bonnieu, S, 2018a. Foam flow in a model porous medium: I. The effect of foam coarsening. Soft. Matter. https://doi.org/10.1039/C7SM01903C.

Jones, S.A., Getrouw, N., Vincent-Bonnieu, S., 2018b. Foam flow in a model porous medium: II. The effect of trapped gas. Soft. Matter. https://doi.org/10.1039/C7SM02458D.

Kam, S.I., Rossen, W.R., 2003. A model for foam generation in homogeneous media. SPE J. https://doi.org/10.2118/87334-PA.

Khoshkalam, Y., Khosravi, M., Rostami, B., 2019. Visual investigation of viscous cross-flow during foam injection in a matrix-fracture system. Phys. Fluids. https://doi.org/10.1063/1.5079482.

Kovscek, A.R., Patzek, T.W., Radke, C.J., 1995. A mechanistic population balance model for transient and steady-state foam flow in Boise sandstone. Chem. Eng. Sci. https://doi.org/10.1016/0009-2509(95)00199-F.

Kovscek, A.R., Radke, C.J., 1994. Fundamentals of Foam transport in porous media. In: foams: fundamentals and applications in the petroleum industry. Adv. Chem. 242, 115–163. American Chemical Society.

Kovscek, A.R., Tang, G.Q., Radke, C.J.: Verification of Roof snap off as a foam-generation mechanism in porous media at steady state. Colloids Surfaces A Physicochem. Eng. Asp. (2007). 10.1016/j.colsurfa.2007.02.035.

Lv, M., Liu, Z., Ji, C., Jia, L., Jiang, Y., 2018. Investigation of pore-scale behaviors of foam flow in a polydimethylsiloxane micromodel. Ind. Eng. Chem. Res. https://doi.org/10.1021/acs.iecr.8b03366.

Marchalot, J., Lambert, J., Cantat, I., Tabeling, P., Jullien, M.C., 2008. 2D foam coarsening in a microfluidic system. EPL Europhys. Lett. https://doi.org/10.1209/0295-5075/83/64006.

Pancharoen, M., Fernø, M., Kovscek, A., 2012. Modeling foam displacement in fractures. J. Pet. Sci. Eng. https://doi.org/10.1016/j.petrol.2012.11.018.

Radke, C.J., Gillis, J.V., 1990. A dual gas tracer technique for determining trapped gas saturation during steady foam flow in porous media. In: Paper Presented at the SPE Annual Technical Conference and Exhibition, New Orleans, Louisiana. /1/1/.

Rangel-German, E.R., Kovscek, A.R., 2006. A micromodel investigation of two-phase matrix-fracture transfer mechanisms. Water Resour. Res. https://doi.org/10.1029/2004wr003918.

Ransohoff, T.C., Radke, C.J., 1988. Mechanisms of foam generation in glass-bead packs. SPE Reserv. Eng. https://doi.org/10.2118/15441-PA.

Rognmo, A.U., Fredriksen, S.B., Alcorn, Z.P., Sharma, M., Føyen, T., Eide, Ø., Graue, A., Fernø, M.: Pore-to-Core EOR upscaling for CO2 foam for CCUS. SPE-190869-PA (2019). 10.2118/190869-PA.

Rossen, W.R.: Foam generation at layer boundaries in porous media. SPE-59395-PA (1999). 10.2118/59395-PA.

Rossen, W.R., 2003. A critical review of Roof snap-off as a mechanism of steady-state foam generation in homogeneous porous media. Colloids Surfaces A Physicochem Eng Asp. https://doi.org/10.1016/S0927-7757(03)00309-1.

Rossen, W.R., Gauglitz, P.A., 1990. Percolation theory of creation and mobilization of foams in porous media. AIChE J. https://doi.org/10.1002/aic.690360807.

Rossen, W.R., Shi, J., Zeilinger, S.C., 1994. Percolation modeling of foam generation in Porous media. AIChE J. https://doi.org/10.1002/aic.690400618.

Saint-Jalmes, A., 2006. Physical chemistry in foam drainage and coarsening. Soft. Matter. https://doi.org/10.1039/B606780H.

Shah, S.Y., Wolf, K.H., Pilus, R.M., Rossen, W.R.: Foam generation by capillary snap-off in flow across a sharp permeability transition. SPE-195310-PA (2019). 10.2118/190210-PA.

Simjoo, M., Zitha, P.L.J., 2020. Modeling and Experimental validation of rheological transition during foam flow in porous media. Transp. Porous Media. https://doi.org/10.1007/s11242-019-01251-9.

Stephenson, D.J., Graham, A.G., Luhning, R.W, 1993. Mobility control experience in the joffre viking miscible CO2 flood. SPE Reserv. Eng. 8 (03), 183–188. https://doi.org/10.2118/23598-pa.

Stone, H.L.: Probability model for estimating three-phase relative permeability. SPE-2116-PA (1970). 10.2118/2116-PA.

Szafranski, R., Lawson, J.B., Hirasaki, G.J., Miller, C.A., Akiya, N., King, .S., Jackson, R. E., Meinardus, H., Londergan, J., 1998. Surfactant/foam process for improved efficiency of aquifer remediation. Structure, Dynamics and Properties of Disperse Colloidal Systems. Darmstadt, pp. 162–167. Steinkopff.

Tang, G.Q., Kovscek, A., 2006. Trapped gas fraction during steady-state foam flow. Transp. Porous Media. https://doi.org/10.1007/s11242-005-6093-4.